



Mn/Co bimetallic catalyst immobilized on N-doped biochar for enhanced photocatalytic degradation of sulfanilamide in water

Honghong Lyu^{a,*}, Xin Wang^a, Pin Li^a, Ping Yan^a, Jingchun Tang^{b,*}

^a Tianjin Key Laboratory of Clean Energy and Pollution Control, School of Energy and Environmental Engineering, Hebei University of Technology, Tianjin 300401, China

^b MOE Key Laboratory of Pollution Processes and Environmental Criteria/Tianjin Engineering Research Center of Environmental Diagnosis and Contamination Remediation, College of Environmental Science and Engineering, Nankai University, Tianjin 300350, China

ARTICLE INFO

Keywords:

Bimetallic photocatalyst
N-doped biochar
Sulfanilamide
Coordination analysis
Degradation mechanism

ABSTRACT

Single-atom catalyst has shown promising effect in photocatalysis. In particular, the construction of bimetallic catalytic sites can address the limitations of single-metallic catalysts, such as clustering and slow electron transfer, which enhances electron transfer between active sites and promotes photocatalytic activity. In this paper, Mn and Co bimetallic catalyst (Mn/Co@N-biochar) was developed by using the electronegativity difference of the bimetallic sites on N-doped biochar to construct catalytically active sites to enhance electron transfer. XRD and HR-TEM characterization confirmed that metal atoms were evenly dispersed within the carbon layer without aggregation or clustering of metal particles. The catalytic efficiency of Mn/Co@N-biochar was assessed through sulfanilamide (SNM) degradation experiments, demonstrating a remarkable degradation rate of 99.3% and a mineralization rate of 49.0%. These values were 10.45 times and 13.24 times more than that for biochar, respectively, indicating that the loading of bimetals greatly improved the photocatalytic activity. Furthermore, the doping of N atoms adjusted the electronic structure of adjacent C atoms and activated the free-flowing π electrons on the biochar surface, creating solid anchoring sites that facilitated efficient electron circulation between Mn and Co atomic sites. The higher local electron density at the Co-N₄ site compared to the Mn-N₄ created electron transfer channels, where Mn atoms (catalytic site) facilitated the flow of electrons to Co atoms (active site). This could rapidly generate the primary active species (·OH and ·O₂) to degrade SNM. Additionally, the stability and applicability of bimetallic catalysts in real water systems were also confirmed, providing valuable insights for the construction of bimetallic biochar structures to degrade organic pollutants in water.

1. Introduction

Sulfanilamide (SNM) is a typical antibiotic pollutant that is difficult to degrade in water, which can be easily absorbed by aquatic plants and pose a hazard to the ecological environment [1,2]. A variety of technologies have been used to degrade antibiotics, among which photocatalytic technology has gained significant attention due to its remarkable degradation efficiency, minimal energy consumption, and absence of any secondary pollution [3]. However, the practical application of this technology has been hindered by slow electron-hole separation and low catalytic efficiency. Therefore, multiple strategies have been devised to improve the catalyst efficiency, including defect control [4], constructing heterostructures [5,6], depositing metal [7], and

doping of atoms [8]. These techniques aim to raise the concentration of carriers and facilitate the charge separation, and ultimately improve the catalytic activity.

Single-atom catalysts (SACs) are considered to be optimal catalysts for enhancing performance by aligning the anchoring position of the substrate [9]. They provide various unique benefits, including a consistent structure at the active site, efficient utilization of metal atoms, exceptional activity, and the capability to bridge the disparity between homogeneous and heterogeneous stages. For example, Dong et al. [10] effectively synthesized Cu single atoms on functionalized COF materials to accomplish complete separation of electrons and holes, which was vital for breaking down sulfamethoxazole. Nonetheless, these catalysts often rely on a solitary metal site to sequentially produce free radicals,

* Corresponding authors.

E-mail addresses: honghonglyu@hebut.edu.cn (H. Lyu), tangjch@nankai.edu.cn (J. Tang).



resulting in a slower recycling efficiency of the generated electrons. To further enhance the rate of charge separation and photocatalytic activity, it has been proposed that constructing multimetallic or bimetallic active sites on the surface of the catalyst could be advantageous. Current research on bimetals predominantly focuses on Pt-Ni[7], Fe-Co[11], Zn-Co[12], and so on. Among these, Mn and Co have garnered significant attention due to its abundance, cost-effectiveness, diverse valence states, rapid reaction kinetics, and robust stability. Neris et al.[13] utilized a catalyst heterojunction comprising Mn and Co, which enhances electron pair separation and boosts redox capacity. However, current research on Mn and Co catalysts is primarily focused on heterojunctions and single-atom catalysts, there is a scarcity of research on enhancing catalytic performance by investigating the Mn/Co bimetallic coordination relationship to establish distinct reaction sites. Hence, it is great importance to study a bimetallic catalyst coordinated by Mn-N4 and Co-N4 to enhance reaction activity.

However, challenges such as nanoparticles and atomic clusters are faced by bimetallic doping. Therefore, it is essential to identify matrixes that are exceptionally stable and disperse, such as metal oxides, MOFs, carbon-based materials[14], and nanomaterials[15], which can be utilized to immobilize and prevent clustering of active metal species. Biochar presents the advantages of high specific surface, excellent electrical conductivity, complex pore structure, abundant functional groups, a substantial number of π -electrons, and a well-formed graphitic structure achieved through controlled pyrolysis temperature[16,17], resulting its broad application prospects in photocatalysis. Incorporating metal nanoparticles into biochar results in the highest level of electrical conductivity, safeguarding specific metals against passivation. Furthermore, biochar contains stable free radicals[18], crucial for generating reactive oxygen species[19]. In addition, element doping (e.g. N and S) can further increase the specific surface area of the material and accelerate charge transfer[20,21]. N rich biochar could further enhance the catalytic activity by donating lone-pair electrons from pyridinic-N and pyrrolic-N to take part in oxidation-reduction reactions. It also provides a stable environment for the high dispersion of monatomic Mn and Co and the formation of electron transfer channels. As a result, N-biochar based metal catalysts find wide application in eradicating antibiotics pollutants.

In this study, biochar-based N-induced bimetallic (Mn and Co) atomic catalysts (Mn/Co@N-biochar) were synthesized using a straightforward and efficient impregnation calcination method. By adjusting the $m(\text{Mn})/m(\text{Co})$ ratio, the study determined the conditions for achieving uniform metal dispersion. Furthermore, we conducted comprehensive stability tests to assess its practical application potential in different ionic and system environments. By X-ray absorption spectroscopy (XAS), we analyzed the coordination environment of the bimetal and explained the reasons behind its efficient degradation effect. Active species capture experiments and electron paramagnetic resonance (EPR) were utilized to evidence the key free radicals involved in the degradation of SNM, thereby uncovering the degradation mechanism and pathway of bimetallic catalytic coordination.

2. Materials and methods

2.1. Materials

Poplar wood chips were purchased from Taiyuan Timber Factory in Tianjin, China. Sulfanilamide (SNM), doxycycline ($\text{C}_{22}\text{H}_{24}\text{N}_2\text{O}_8$), erbium (ER), melamine ($\text{C}_3\text{H}_6\text{N}_6$), ethylenediaminetetraacetic acid disodium salt (EDTA-2Na) and sodium chloride (NaCl) were purchased from Shanghai Aladdin Biochemical Technology Co., Ltd, and was described in detail in Section 1 of Supporting Information (SI).

2.2. Synthesis of Mn/Co@N-biochar catalysts

The poplar wood chips were crushed and those with a diameter of

less than 3 mm were screened out. Then, the obtained material was dried in an oven at 80 °C for 8 hours. The biochar was prepared by heating the material at 500 °C for 3 hours under nitrogen atmosphere in a tube furnace (CY-TU1400C-M, Hunan Changyi Microwave Technology Co., Ltd., Hunan, China). The bimetallic carbon material was prepared through impregnation and calcination. A mixture of 0.6 g of biochar, 0.11 mmol of $\text{MnCl}_2 \cdot 4 \text{ H}_2\text{O}$, 0.29 mmol of $\text{Co}(\text{NO}_3)_2$, and 12.07 mg of $\text{C}_6\text{H}_{12}\text{O}_6$ was added to 50 ml of deionized water and ultrasonicated for 1 hour. The ratio of $m(\text{Mn}/\text{Co})$: $m(\text{biochar})$ was 1:15. The resulting solution was freeze-dried in a freeze-drying apparatus (FD-1B-50, Beijing Biocool Experimental Instrument Co., Ltd., Beijing, China). The dried material and Melamine were mixed uniformly with a mass ratio of 1:5 and calcined in a tube furnace at a temperature of 800 °C and a N_2 atmosphere for 2 hours to synthesize the bimetallic at N-doped biochar material (Mn/Co@N-biochar). Additionally, a series of samples with different $m(\text{Mn})$: $m(\text{Co})$ ratios were synthesized using the same method. Details are shown in Table S1.

2.3. Characterization of Mn/Co@N-biochar

Samples were analyzed for elements and crystal structure using X-ray diffraction (XRD) (Bruke D8 Advance). The morphology of the samples and the internal structure of the crystals, atomic sequences were presented by field emission scanning electron microscopy (SEM) (Hitachi Regulus8100) and using high resolution transmission electron microscopy (HR-TEM) (FEI TECNAI G2 F20), respectively. The arrangement of Mn and Co atoms was assessed using aberration-corrected high-angle annular dark-field scanning transmission electron microscopy (HAADF-STEM). The coordination structures and chemical valence states of Mn and Co atoms were evaluated by X-ray absorption spectroscopy (XAS) and X-ray photoelectron spectroscopy (XPS) (Thermo ESCALAB 250XI). The photoelectric signal intensity of the material was measured by electrochemical impedance spectroscopy (EIS) (CS310H, Wuhan Kaiset Instrument Co., Ltd., Wuhan, China), transient photocurrent response (CHI660E, Shanghai Chenhua Instrument Co., Ltd., Shanghai, China), linear sweep voltammetry (LSV) (0.5 M sodium sulphate solution), and photoluminescence (PL) (F-4600 Hitachi, Japan). Fourier transform infrared spectroscopy (FTIR) (Bruker Vertex 70) was used to analyze the changes of surface functional groups before and after the synthesis of the catalysts. The adsorption-desorption isotherm (Autosorb-iQ, Quantachrome) enabled the determination of the pore diameter distribution and specific surface area (SSA) of the given samples. Free radical signals (including $\cdot\text{O}_2$ and $\cdot\text{OH}$) were measured using an electron paramagnetic resonance (EPR) spectrometer (Bruker, EMXplus).

2.4. Photocatalytic degradation of SNM

A prepared water solution containing SNM (10 mg/l, 10 ml) and Mn/Co@N-biochar catalyst (1 g/l, 0.01 g) was introduced into the photocatalytic reaction tube. The contents were mixed thoroughly using Ultrasonic Cleaner. The photocatalytic photoreaction device (PhchemIII, Beijing New Bit Technology Co., Ltd., Beijing, China) was used, along with the magnetic stirring system and cooling system, to ensure a sufficient reaction and maintain the reaction temperature at 23 °C. To reach adsorption-desorption equilibrium before photocatalytic reaction, the mixture was first allowed to react without light for 30 minutes. Then, a xenon lamp with a wavelength of 420 nm and a power of 450 W was activated to initiate the illumination reaction, which lasted for 6 h. After the reaction, the mixture was filtrated using a nylon syringe filter with a pore size of 0.22 μm . The concentration of SNM present in the filtrate was then measured using a UV spectrophotometer

To explore the influence of catalyst dosage on the efficacy of SNM removal, varied dose (2.5 mg, 4 mg, 5 mg, 7.5 mg, 10 mg, and 12 mg) of Mn/Co@N-biochar catalysts were combined with a 10 ml solution of SNM (10 mg/l) under the initial pH value of 6.8. The photocatalytic reaction was then conducted to measure the remaining SNM

concentration. To investigate the effect of solution pH on the degradation of SNM, 10 mg Mn/Co@N-biochar was added to 10 ml of solution containing SNM (10 mg/l), then NaOH (1 M) or HCl (0.1 M) was utilized to adjust the pH of the original solution to 2–11.

2.5. Methods for SNM analysis DFT calculation

A UV-visible spectrophotometer (UV-1801, Beijing Beifen Ruili Analyzer Co., Ltd., Beijing, China) was used to measure the absorbance of SNM at its peak absorption wavelength of 260 nm, and the concentration of SNM was counted by substituting into the pre-fitted standard curve. Gaussian software package was used to calculate and analyze the DFT values, and was described in detail in [Section 2 of Supporting Information \(SI\)](#).

3. Results and discussions

3.1. Synthesis and characterization

[Fig. 1a](#) presents the synthesis process of Mn/Co@N-biochar. In brief, metallic Mn and Co precursors were impregnated into the biochar structure, which was then subjected to N doping using $C_3H_6N_6$. The subsequent high-temperature calcination process effectively eliminated organic solvents and securely embedded Mn, Co, and N atoms within the carbon structure. It is worth mentioning that we added an appropriate amount of glucose during the doping process of Mn and Co to enrich the carbon structure of biochar, enhance the conductivity of the material [\[22,23\]](#), and improve the ability to oxidize SNM. We prepared three different materials: Mn, Co, and N-doped glucose (Mn/Co@N-G),

Mn/Co@N-BC (without $C_6H_{12}O_6$), and Mn/Co@N-biochar. The results of the experiment on SNM removal indicated that Mn/Co@N-G had a significantly higher adsorption rate than the catalytic rate ([Fig. 1b](#)), with values of 62.60% and 17.80% respectively. Additionally, the adsorption rate and removal rate of Mn/Co@N-biochar increased by 2.02% and 13.03% respectively compared to Mn/Co@N-BC. These results suggested that the introduction of $C_6H_{12}O_6$ improved the adsorption capacity of Mn/Co@N-biochar for SNM, resulting in better interaction with active sites and ultimately enhancing the photocatalytic effect.

The electron-acquisition capacity (EAC) and electron-donation capacity (EDC) of catalysts were analyzed using mediated electrochemistry ([Fig. 1c, d](#) and [Fig. S1](#)). The Mn/Co@N-biochar exhibited an electron-receiving ability of $0.832 \text{ mmol e}^- (\text{g biochar})^{-1}$, and an electron-donating ability of $0.92 \text{ mmol e}^- (\text{g biochar})^{-1}$, which was higher than those of Mn/Co@N-BC (EAC = $0.78 \text{ mmol e}^- (\text{g biochar})^{-1}$, EDC = $0.84 \text{ mmol e}^- (\text{g biochar})^{-1}$), indicating that the inclusion of $C_6H_{12}O_6$ effectively improved the redox capacity of Mn/Co@N-biochar [\[24\]](#). The electron-accepting groups within Mn/Co@N-biochar (mostly carbon groups and quinones) [\[25\]](#), directly trapped electrons in SNM to enhance the oxidation process. Currently, the electron-donating groups mediated the reduction of dissolved molecular oxygen to active oxygen (ROS, $\cdot O_2^-$) [\[26\]](#), thereby facilitating SNM oxidation in water and promoting the adsorption of SNM on the Mn/Co@N-biochar surface, and indirectly boosting the catalytic oxidation capability of the catalyst. For further study of the experiment, N-biochar with different weight ratios of Mn: Co (0:1, 0.1:0.9, 0.3:0.7, 0.5:0.5, 0.7:0.3, 0.9:0.1, and 1:0) were prepared during the doping process.

XRD pattern ([Fig. S2](#)) confirmed that Mn and Co incorporation did not alter the crystal structure of pristine biochar. Morphological state of

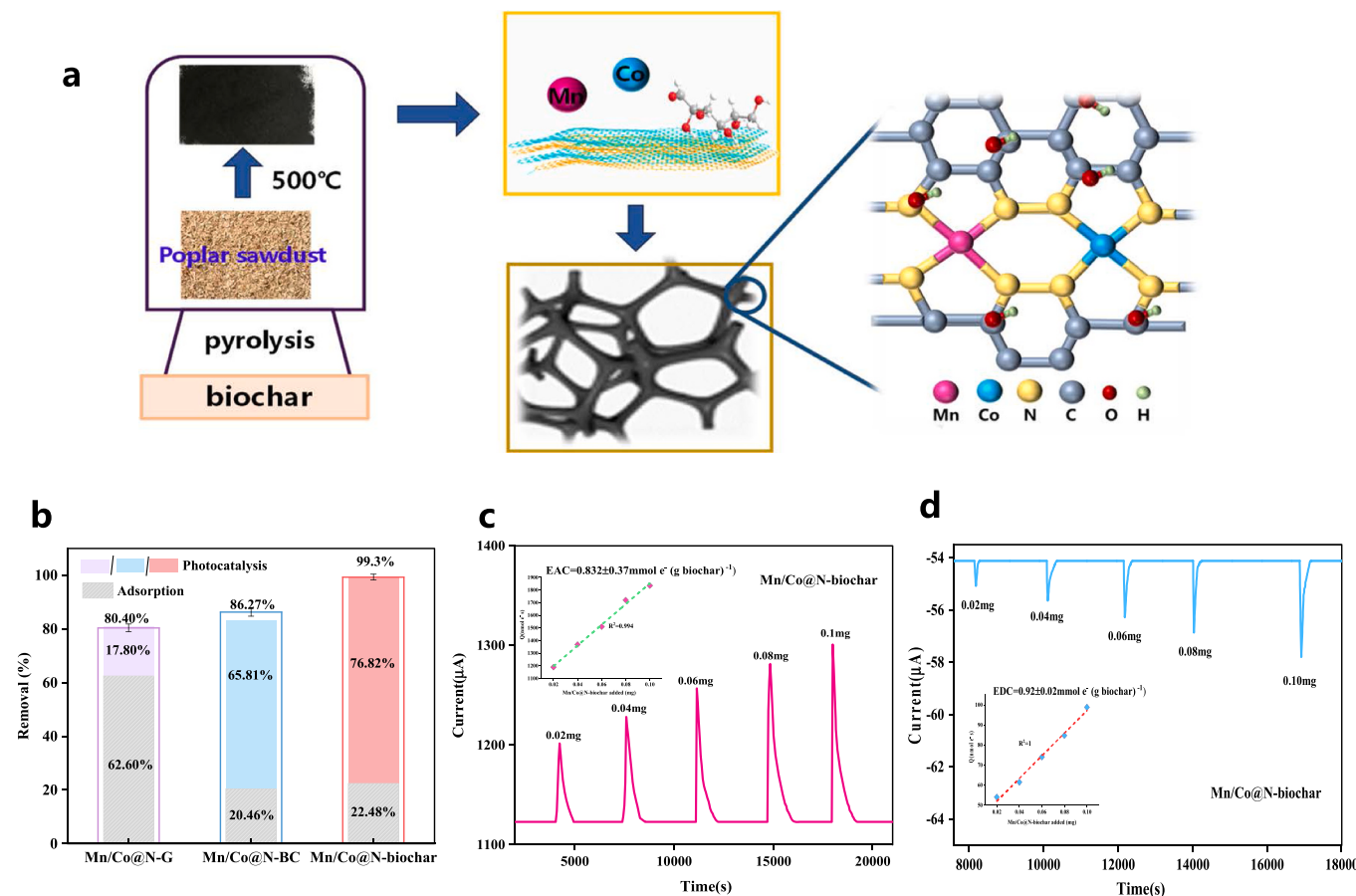


Fig. 1. (a) Diagram of the preparation process of Mn/Co@N-biochar. (b) Photocatalytic experiments on SNM removal by Mn/Co@N-biochar, Mn/Co@N-BC, and Mn/Co@N-G. Mn/Co@N-biochar mediated reduction curves (c) and oxidation curves (d), and the inset contains the integrated peak area plotted according to Mn/Co@N-biochar and the corresponding EAC and EDC values.

biochar and Mn/Co@N-biochar was observed by SEM. Fig. 2a-b showed that original biochar had a high pore density, providing numerous anchoring locations for metals[25]. In contrast, the Mn/Co@N-biochar exhibited a distinct arrangement of pore structure with open pores (Fig. 2c-d), demonstrating that the optimization method did not disrupt the transcend and unrivaled pore structure of the original biochar. Additionally, the modification process required high temperature pyrolysis, which opened up the occluded pore structure of the biochar. This increase in pore size enhanced the contact area with SNM and provided more extensive surface area for catalytic reactions, thereby improving the catalytic performance.

As shown in Fig. 2e, the HR-TEM imaging of the biochar revealed the coexistence of carbonized and disordered structures, creating a precondition for the successful adding of Mn and Co[21]. The presence of lattice streaked corresponding to the (002)[26,27] structure, from the HR-TEM images of Mn/Co@N-biochar (Fig. 2f), was in accordance to the results of XRD analysis. In addition, no metal nanoparticles were recognized in the HR-TEM imaging, and only biochar was visible in selected area electron diffraction (SAED)[12], the formation of metal particles/compounds could be further ruled out. The dispersion of atoms in Mn/Co@N-biochar could be effectively visualized through HAADF-STEM and TEM element mappings. In Fig. 2g, the distinct bright spots correspond to Mn/Co atoms, indicating a uniform distribution of metal atoms in Mn/Co@N-biochar. Fig. 2h provided further evidence for the distribution of Mn and Co elements at the atomic level in N-doped carbon substrates. Furthermore, when combined with the EDS distribution of Mn@N-biochar and Co@N-biochar (Fig. S3), the dispersion of

Mn and Co on the biochar surface was also confirmed.

The valence and coordination environments of metal atoms can be better understood through x-ray absorption spectroscopy (XAS) measurements. As seen in the XANES spectrum of Mn/Co@N-biochar (Fig. 3a), it became apparent that the absorption energy near the Mn K-edge corresponded to a valence state between Mn foil and MnO. This suggested that Mn atoms carried a positive charge while exhibiting an oxidation state between Mn^0 and Mn^{2+} . Similarly, comparing spectra of Co using x-ray absorption near-edge structure (XANES), we were able to establish that the atoms at the absorption edge fell between Co foil and CoO (Fig. 3b). Therefore, the valence state of Co atoms ranges from 0 to 2^+ . It could be hypothesized that the consumption of electrons by nearby N atoms via valence bonds could be the reason behind the positive charge centers in Mn and Co[28]. Additionally, a deeper understanding of the coordination environment can be obtained by evaluating the k^3 -weighted Fourier transform (FT) of the EXAFS at the Mn and Co K-edges (Fig. 3c, d). At the Mn and Co edges, the scattering paths of Mn-N and Co-N displayed prominent peaks at 1.5 Å[29] and 1.53 Å[30], respectively, indicating their coordination relationships. In contrast, the absence of peaks near 2.6 Å (Mn-Mn bond) and 2.49 Å (Co-Co bond) [31] confirmed the lack of Mn or Co atom clusters in the Mn/Co@N-biochar. The EXAFS fitting of Mn/Co@N-biochar results revealed that Mn and Co atoms were dispersed throughout the sample, and the metal atoms coordinated to the N atoms. The Mn-N bond measures 2.18 Å in length, with a coordination number of approximately 3.7, while the Co-N bond has a length of 1.98 Å and a coordination number of roughly 4 (Fig. 3e, f, and Table S2)). Additionally,

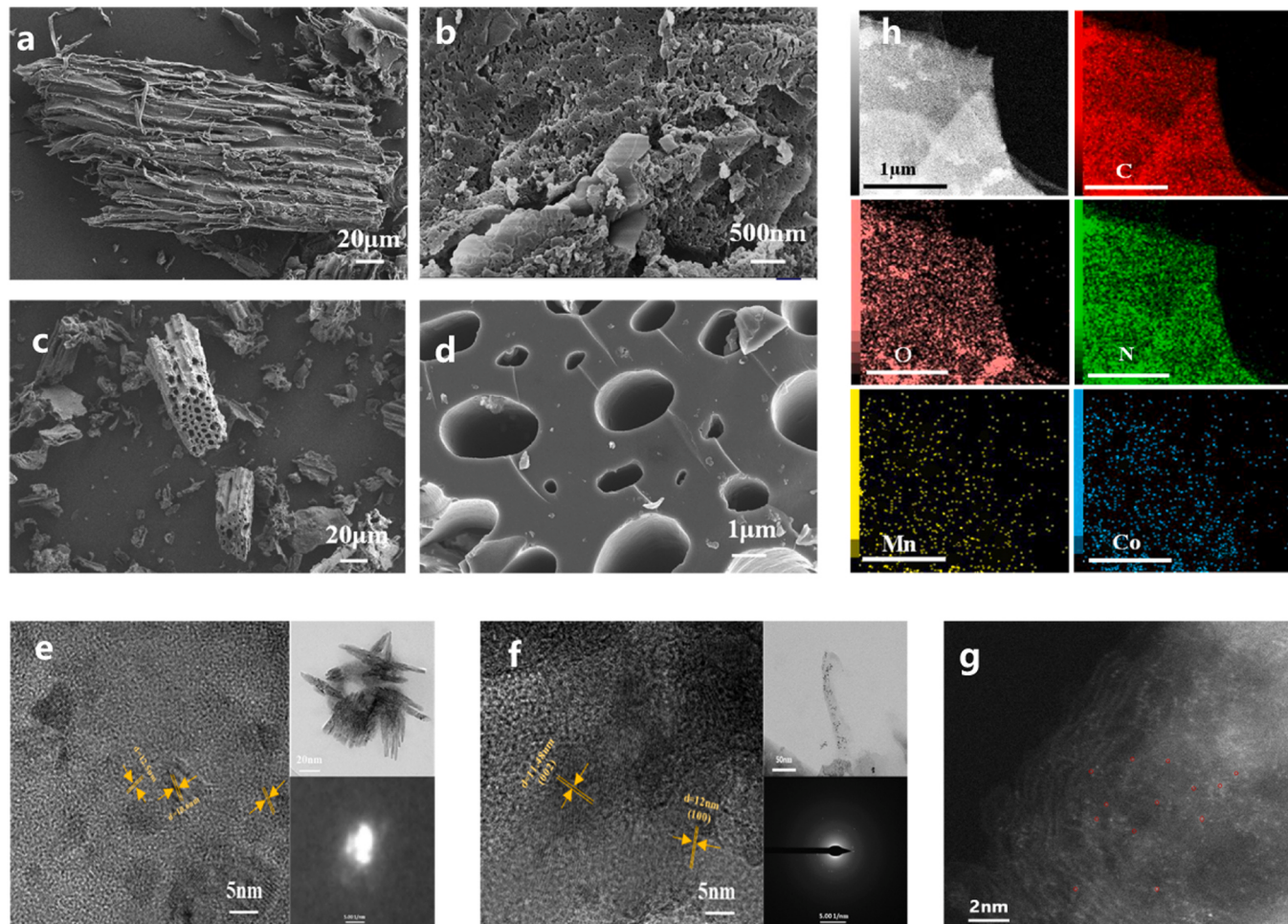


Fig. 2. (a-d) SEM images of biochar (a), Mn/Co@N-biochar (c), and high-magnification images of biochar (b), Mn/Co@N-biochar (d). (e-f) HR-TEM imaging of biochar (e) and Mn/Co@N-biochar (f). (g) HAADF-STEM imaging of Mn/Co@N-biochar. (h) TEM EDS mapping images of C, O, N, Mn, and Co in Mn/Co@N-biochar.

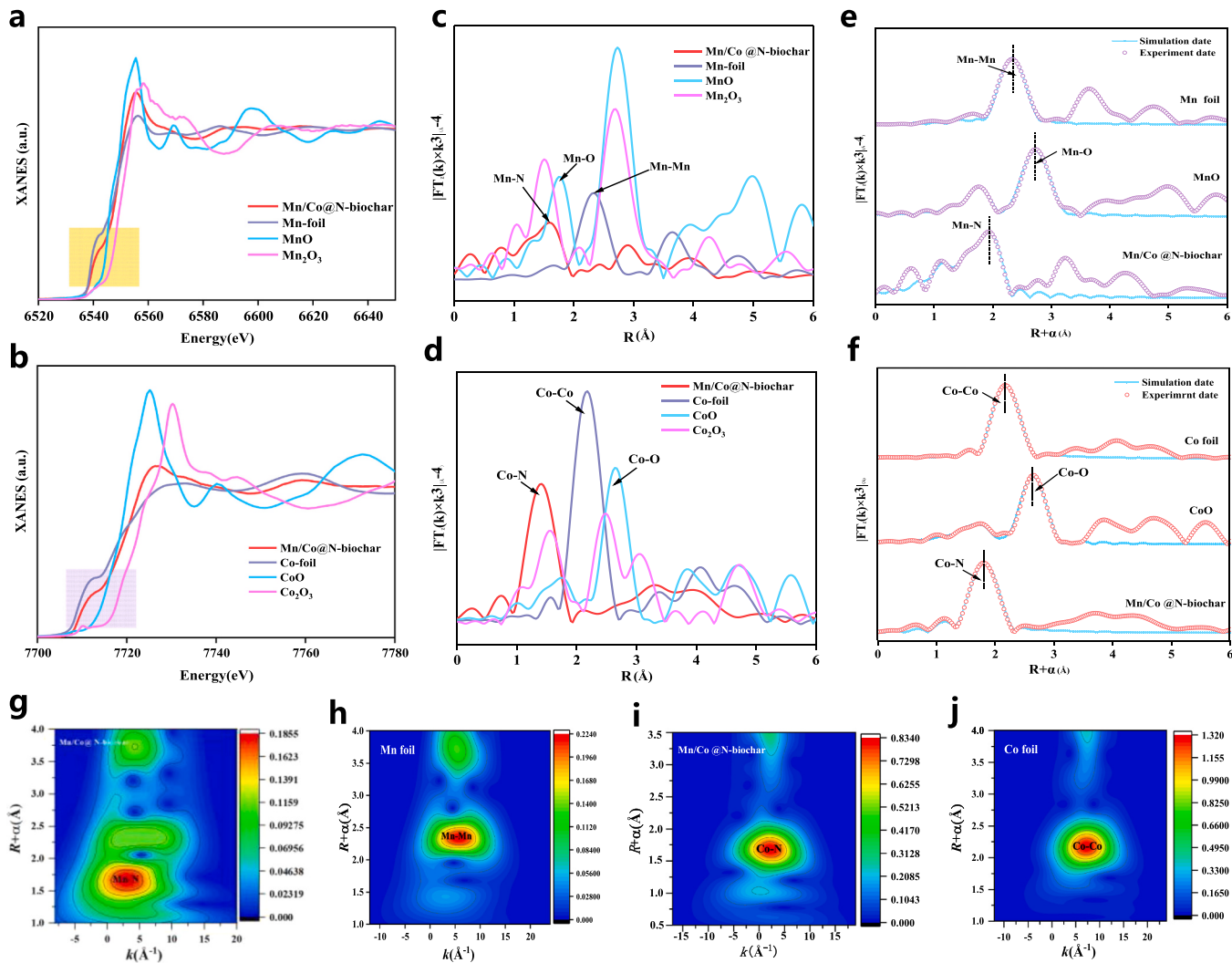


Fig. 3. XANES spectrum of Mn/Co@N-biochar at (a) Mn K-edge and (b) Co K-edge. FT k^3 -weighted EXAFS spectrum of Mn/Co@N-biochar at (c) Mn K-edge and (d) Co K-edge. EXAFS fitting curves of at (e) Mn K-edge and (f) Co K-edge. (g-j) Wavelet transform of the k^3 -weighted EXAFS data of the Mn K-edge of Mn/Co@N-biochar (g), Mn foil (h), the Co K-edge of Mn/Co@N-biochar (i) and Co foil (j).

through the application of EXAFS wavelet transformation (WT) examination on Mn/Co@N-biochar (Fig. 3g, i), we detected the highest intensity in the WT map of Mn/Co@N-biochar at approximately 4.0 \AA^{-1} , aligning with Mn-N and Co-N coordination [32]. The WT diagrams of Mn foil, MnO, Co foil, and CoO exhibited no tangible peak intensity associated with Mn-Mn and Co-Co contributions (Fig. 3h, j, and Fig. S4a, b). Synthesizing the findings from the HAADF-STEM observations and EXAFS analysis, we can assert that individual Mn and Co atoms are present at the Mn-N₄ and Co-N₄ sites, respectively.

XPS was utilized to analyze the surface components of the samples and determine the valence states of metals. The valence states of the atoms within the material along with the distribution of the chemical bonds were shown in Fig. 4a-f. Furthermore, Table S3 presented that the surface of the catalyst contains varying concentrations of atoms. Following the observation of Fig. 4a, we identified the existence of elements C, N, O, Mn, and Co in the Mn/Co@N-biochar, which aligns with our initial expectations. To gain further insight, Fig. 4b elucidated the results of high-resolution C 1 s spectra, revealing three noticeable peaks at 284.18 eV, 284.83 eV, and 285.76 eV. These peaks correspond to the existence of C-C/C-N [33], C-C, and C-O/C=N bonds, respectively. The occurrence of C-N and C=N bonds validates the replacement of N atoms for some of the C atoms in the biochar, indicating successfully N-doping. To examine the oxygen bonding in more detail, Fig. 4c displayed the

high-resolution O 1 s spectra, exhibiting two peaks at 531.5 eV and 532.49 eV, which correspond to the O-C=O and C-O chemical bonds, respectively [21]. As shown in Fig. 4d, the Mn 2p XPS spectra of Mn/Co@N-biochar revealed peaks at 641.43 eV and 653.29 eV, representing the binding capacity of Mn 2p_{3/2} and Mn 2p_{1/2}, respectively. The Mn 2p_{3/2} peak's proximity to Mn²⁺ indicated a Mn valence state of +2 in Mn/Co@N-biochar. A detailed deconvolution of the Co 2p XPS spectrum (Fig. 4e) identified binding energy of 780.5 eV and 796.5 eV, corresponding to Co 2p_{3/2} and Co 2p_{1/2} peaks. Additionally, peaks at 784.3 eV and 800.5 eV were characteristic of Co 2p_{3/2} and Co 2p_{1/2}, confirming the presence of divalent Co [34]. The composition of N species in Mn/Co@N-biochar was determined in Fig. 4f, which included pyridine-N, graphitic-N, imental-N, pyrrole-N, and oxidized-N [16, 35]. Each of these species was observed as distinct peaks at 397.8, 399.7, 400.75, and 402.2 eV, respectively. Co-N and Mn-N were resulted from the bonding of N atoms with Co and Mn atoms, as evidenced by the corresponding peaks present in the Co 2p and Mn 2p XPS spectra. This was in agreement with the XAS analysis result of coordinated MnN₄ and CoN₄. This observation implied that the electronic structure was influenced and properties of the biochar were optimized by the existence of Mn and Co. Moreover, enhancing the abundance of active sites was accomplished by aligning the electronic structure of C via N doping to create stable coordination sites [36].

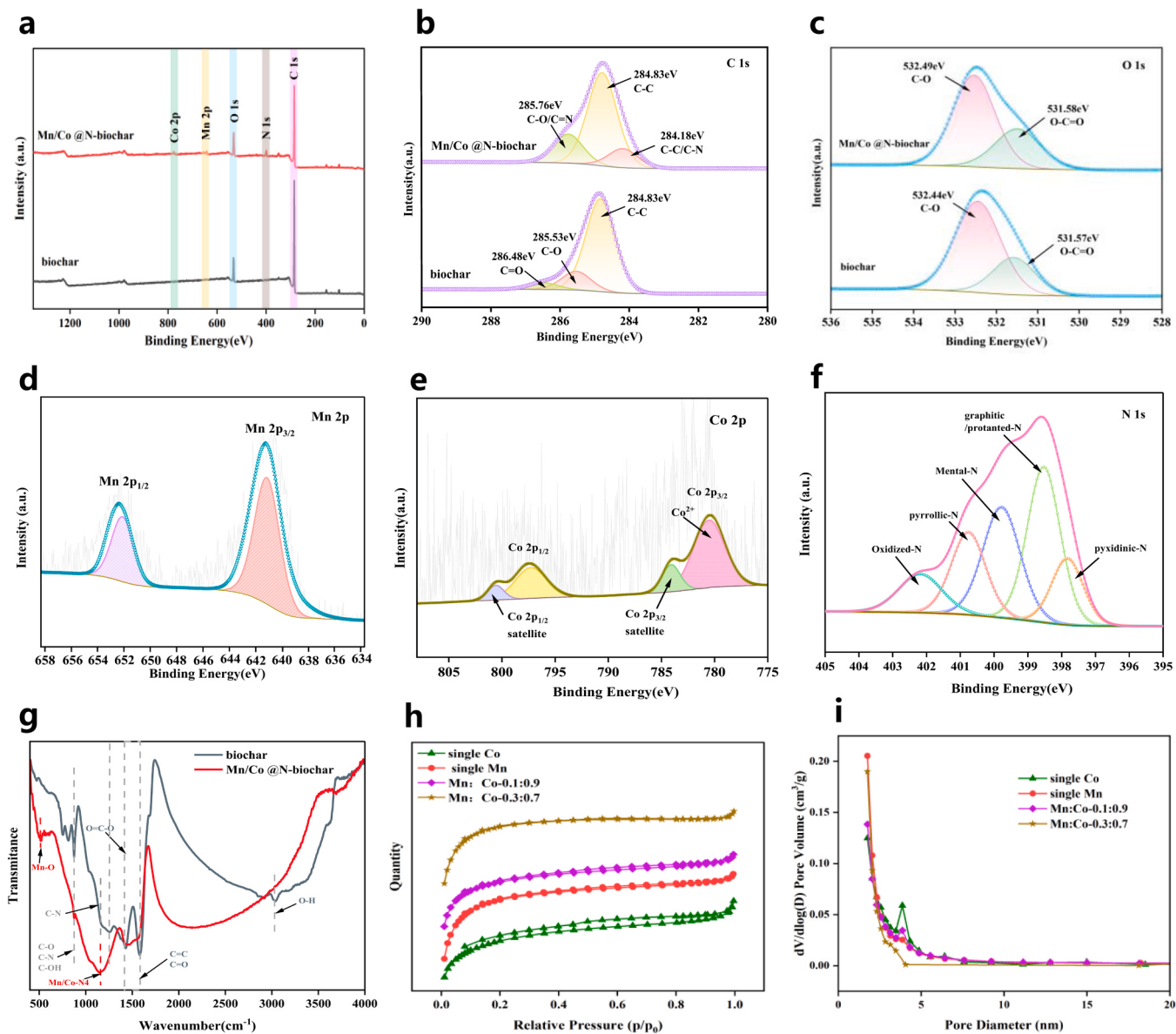


Fig. 4. (a) Full scan XPS spectra of biochar and Mn/Co@N-biochar. (b-c) XPS spectrum of biochar and Mn/Co@N-biochar: C 1 s (b) and O 1 s (c). (d-f) XPS spectrum of Mn/Co@N-biochar: Mn 2p (d), Co 2p (e), and N1s (f). (g) FTIR spectra of biochar and Mn/Co@N-biochar. N₂ adsorption-desorption isotherms (h) and pore diameter distributions (i) of biochar and Mn/Co@N-biochar.

FTIR spectroscopy was utilized to study the functional groups and internal structural changes arising in biochar and Mn/Co@N-biochar materials. As illustrated in Fig. 4g, the characteristic absorption bands of Mn elemental doping was appeared at 518 cm⁻¹ and could be attributed to the stretching vibrations of metal-oxygen bonds[37], and the stretching vibrations of the materials at 876 cm⁻¹, 1414 cm⁻¹, and 1590 cm⁻¹ correspond to the distinctive peaks of C=O, O=C=O, and C-C/C=O, respectively. Notably, noteworthy enhancements were noted in the -OH stretching of hydroxyl groups bonded (3026 cm⁻¹) and the stretching of quinone group C=O (1487 cm⁻¹) in Mn/Co@N-biochar in comparison to biochar. This occurrence could be due to the pore-opening effect of the calcination process, which exposed a greater number of functional groups on the surface of the biochar. Furthermore, the existence of the quinone group (C=O) augments the electron transfer capacity and strengthens the oxidation reaction[38]. Upon doping Mn/Co atoms into the catalysts, a notable increase in the characteristic absorption peak at 1155 cm⁻¹ was observed, suggesting the formation of Mn/Co-N₄ bonds through direct bonding with N atoms

[39]. Furthermore, the presence of peak at 1160 cm⁻¹ in Mn/Co@N-biochar indicated successful incorporation of N atoms into the carbon network structure of the biochar. The isotherms and curves of nitrogen adsorption-desorption were evaluated for biochar composites containing different loading ratios of Mn and Co, as displayed in Fig. 4h-i. In accordance with the guidelines of IUPAC (International Union of Pure and Applied Chemistry)[40,41], the nitrogen adsorption isotherm illustrated in Fig. 4h showed a type I isotherm, corroborating the microporous structure of these materials. Despite the prevalence of micropores in the adsorption-desorption isotherm with an increase in Co ratio, its shape gradually transitions towards an IV type isotherm characterized by the H3 hysteresis loop. The relative pressure (P/P₀) of the hysteresis loop spans from 0.1 to 1.0, indicating the presence of medium or large holes. This finding is further reinforced by the analysis of pore size distribution (Fig. 4i). The peaks of the pore size distribution across all samples fall within the range of 0.5–5 nm, which confirms the existence of micropores and small mesopores in the material[42]. These pores served as channels for effective adsorption and catalytic

degradation of SNM[43]. It was important to mention that the SEM image of Mn/Co@N-biochar displayed a pore size of 1 μm , while the N_2 adsorption-desorption isotherm and pore size distribution analyses indicated smaller pore sizes (0.5–5 nm). This difference could be due to the complex pore structure of biochar at various scales. The SEM focused on the surface microstructure, leading to the detection of larger pores, whereas the N_2 adsorption-desorption isotherms provided insight into the internal pore arrangement. Specifically, N_2 was highly sensitive to the microporous and mesoporous configurations, resulting in isotherms suggesting smaller pore sizes. Therefore, to fully assess the pore characteristics of Mn/Co@N-biochar, a comprehensive analysis combining SEM images and N_2 adsorption-desorption isotherms was necessary. From Table S4, it was observed that the specific surface area of biochar burdened with single Mn or single Co was lower than that of loaded bimetals. This was because, during the pyrolysis process, individual atom was prone to aggregate into chemically stable clusters or nanoparticles, which imposed limitations on the advancement and practicality of SACs. However, when the Mn and Co loadings were adjusted, a more superior structure was displayed, indicating an important relationship between the degradation performance and the Mn:Co loading ratio.

3.2. Photocatalytic performance

In the initial stage of the Mn/Co@N-biochar catalyst synthesis, the precursor solution's weight ratios of Mn: Co were adjusted as the optimum synthesis conditions. The ratios tested were 0.1:0.9, 0.3:0.7, 0.5:0.5, 0.7:0.3, and 0.9:0.1, respectively. In the study depicted by Fig. 5a, it was observed that the utmost catalytic efficiency of 99.3% was attained when the ratio of m(Mn):m(Co) was 0.3:0.7. As the Mn: Co ratio increased, the degradation of SNM gradually decreased. This suggested that the removal rate of SNM was closely linked to the actual m(Mn):m(Co) ratio of the materials. Combined with the results of XAS analysis, it could be revealed that the Co atoms in the Mn/Co@N-biochar (m(Mn):m(Co)=0.3:0.7) were dispersed, while the Mn atoms exhibited inconspicuous clustering, which suggested that if the Mn content is further increased it may lead to the aggregation of Mn atoms to form clusters or nanoparticles, which was not conducive to the photodegradation activity. Based on this analysis, the optimum m(Mn):m(Co) ratio for SNM degradation was determined to be 0.3:0.7, making it the ideal experimental material (Mn/Co@N-biochar) for subsequent studies. Under both conditions of complete darkness and light, an evaluation was conducted to assess the efficacy of SNM removal by biochar, N-biochar,

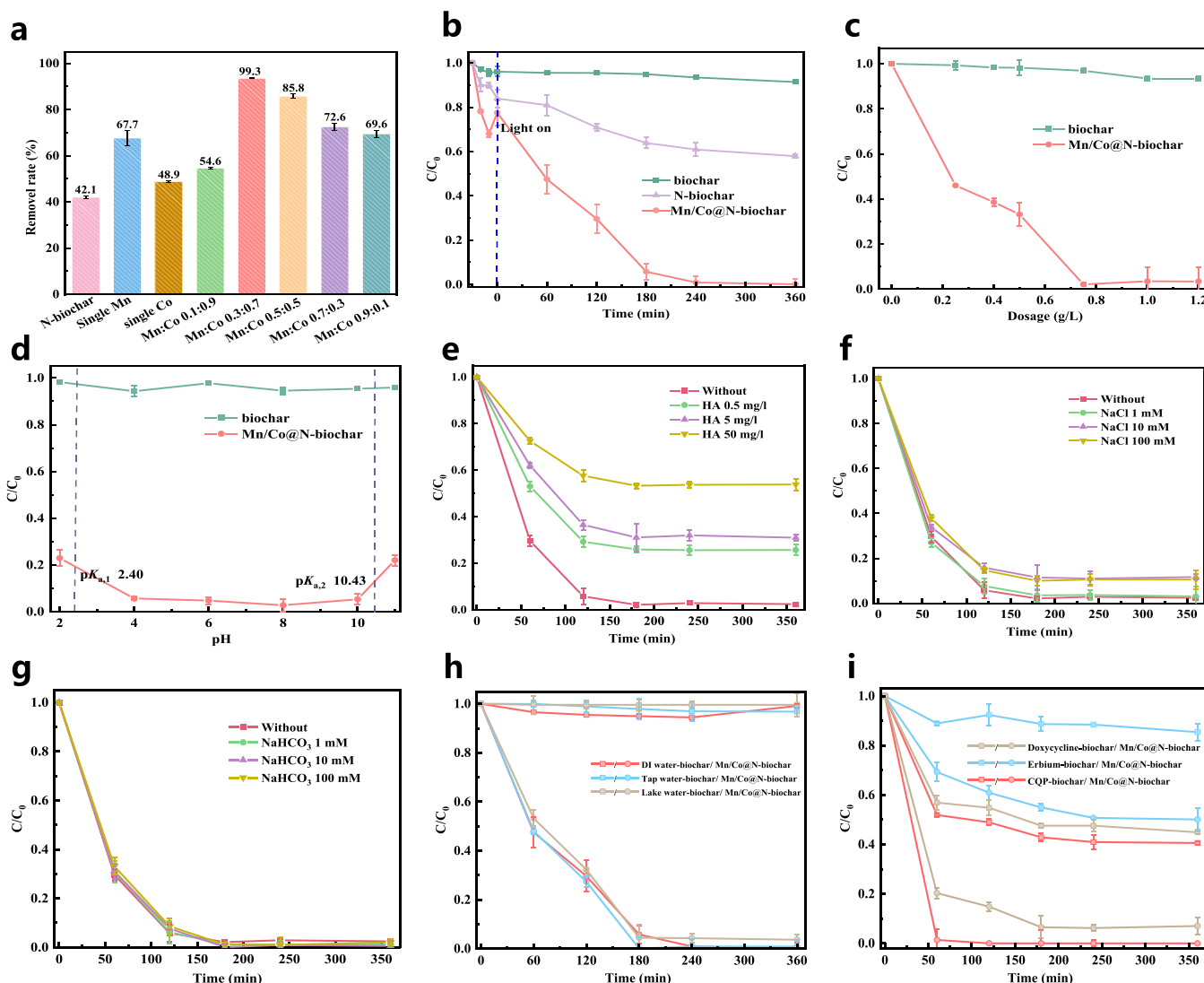


Fig. 5. (a) SNM degradation performance of materials prepared with different Mn: Co ratios. (b) The influence of reaction time on the removal of SNM by biochar, N-biochar and Mn/Co@N-biochar under both dark and light conditions. (c-d) Influence of change catalyst dosage (c) and solution pH (d) on the degradation of SNM in biochar and Mn/Co@N-biochar. (e-g) The effect of different impurities of HA (e), Cl⁻ (f) and HCO₃⁻ (g) on the degradation of Mn/Co@N-biochar by SNM. (h-i) The impact of actual water samples (h) and various antibiotics (i) on the degradation of biochar and Mn/Co@N-biochar.

and Mn/Co@N-biochar (Fig. 5b). Among these, only the biochar reaction system showed difficulty in degrading SNM, with both the N-biochar and Mn/Co@N-biochar reaching a state of adsorption-desorption equilibria after 30 minutes. The adsorption rate percentages were 2.92%, 12.3%, and 22.5% observed for biochar, N-biochar and Mn/Co@N-biochar, respectively, indicating the adsorption efficiency of Mn/Co@N-biochar on SNM was significantly improved. The efficient accumulation of pollutants on the photocatalyst facilitated the subsequent photodegradation process. This study analyzed the photocatalytic behavior of three materials in degrading SNM under light exposure. After 6 h of light exposure, the degradation effect of N-biochar increased from 9.5% to 42.1%. This could be attributed to the addition of N atoms modulated the electronic structure of adjacent C atoms, increasing the number of positive charges, thereby accelerating the generation of free radicals. Alternatively, the N atoms directly received electrons from SNM, leading to the degradation of SNM[44]. Furthermore, upon the doping of Mn and Co, the degradation rate significantly increased to 99.3%. This indicated that the electronegativity difference between Mn and Co promoted electron circulation, thereby extending the lifetime of photoexcited carriers and accelerating the kinetic reaction rate of SNM degradation.

The analysis focused on the influence of catalyst dosage (Fig. 5c) on the degradation process of SNM. As the dosage of catalyst was increased from 0.2 g/l to 1 g/l, the photodegradation rates of SNM by biochar and Mn/Co@N-biochar experienced increase from 3.9% to 9.5% and from 64.0% to 99.3%, respectively. This could be connected to the generation of a greater concentration of free radicals with an increased amount of catalyst, which fulfilled the requirement for degrading pollutants[45]. Nevertheless, as the concentration rose beyond 1 g/l to 1.2 g/l, a decrease in the elimination efficiency was observed, indicating that a higher catalyst dosage did not necessarily yield better results. This was because the high concentration of catalyst led to light scattering, preventing effective contact between light and SNM. Henceforth, an optimum dosage of 1 g/l of Mn/Co@N-biochar was established and deemed suitable for forthcoming experiments. Fig. 5d illustrated the effect of pH on the removal of SNM. Initially, the elimination of SNM escalated, but later declined with an augment in the pH value. The utmost rate of removal was observed at pH values ranging from 4 to 8. However, the degradation rate of SNM decreased under excessively acidic and alkaline conditions. This could be attributed to the ionization of SNM, which contains two basic groups (-NH₂)[46]. At different pH values, SNM exists in different forms, with pKa values of 2.40 (pKa, 1) and 10.43 (pKa, 2)[47]. When the pH dropped below 2.40, the SNM molecules became positively charged, while at pH values exceeding 10.43, they acquired a negative charge. Between pH values of 2.40 and 10.43, SNM molecules were electrically neutral. The zero-point values of biochar and Mn/Co@N-biochar were analyzed to be 3.32 and 5.21, respectively (Fig. S5). Adsorption under highly acidic and alkaline conditions was found to be poor and unfavorable for SNM degradation due to electrostatic repulsion. At pH levels of 2 and 11, the removal efficiency of Mn/Co@N-biochar in terms of SNM decreased to 78.5% and 75.0%, respectively. Furthermore, the existence of -OH in biochar and Mn/Co@N-biochar facilitated the creation of hydrogen bonding with the electronegative elements (e.g., N and O)[46] in SNM, enhancing its adsorption ability. However, In the presence of extremely acidic conditions, the negatively charged oxygen-containing functional groups on the biochar and Mn/Co@N-biochar became protonated[48], resulting in a loss of hydrogen bonding and limiting the adsorption of SNM. By considering the presence of organic ions and other accompanying ions in the actual water environment, this experiment investigated the impact of Mn/Co@N-biochar on SNM degradation under conditions containing typical organic matter and coexisting ions, such as HA, HCO₃⁻, and Cl⁻. Fig. 5e displayed the outcomes that demonstrated a significantly inhibition in the photocatalytic removal of SNM when HA was introduced into the solution. As the HA concentration rose from 0 mg/l to 50 mg/l, the SNM removal rate witnessed a decline from 99.3% to 41.4%. This

effect was linked to that HA competed with SNM for -OH and -O₂ radicals required for degradation[49]. Another factor could be the presence of functional groups in HA, including phenolic, hydroxyl, and carboxyl groups, resulted in significant obstruction of the active sites on the surface of Mn/Co@N-biochar. This obstruction ultimately decreases the chances of adsorption and degradation of SNM. Moreover, research had also demonstrated that HA creates surface complexes that adhere to the catalyst surface[50], thereby influencing the subsequent reaction between SNM molecules and the catalyst. Fig. 5f-g depicted the distinct impact of inorganic anions on the photodegradation of SNM. Interestingly, the presence of Cl⁻ inhibited the degradation process of SNM, reducing the degradation rate from 99.3% to 89.0%. It is suggested that as the Cl⁻ concentration increased, it scavenged h⁺ and -OH radicals and produced less active chlorine species (•Cl₂) (Eqs. (1-2))[51], which, in turn, somewhat inhibited the degradation of SNM. Nonetheless, when HCO₃⁻ was introduced, the removal of SNM experienced a slight enhancement, exhibiting an increased degradation rate from 99.3% to 99.8%. This particular result could be attributed to the reaction between HCO₃⁻ and -OH, forming CO₃²⁻ (Eq. (3)). Though CO₃²⁻ as a secondary radical showed a lower reaction rate compared to -OH, it facilitated the oxidation of N-containing organic pollutants[52,53].



To investigate the impact of Mn/Co@N-biochar in practical applications, we conducted degradation experiments on SNM using actual water samples sourced from both lake and tap water (Fig. 5h). Although the degradation efficiency of SNM in real water was lower than that of deionized water reaction system (with a degradation rate of 99.3%), the degradation rates achieved were still notable, measuring at 95.4% and 97.4%, respectively. This indicated that the diminished removal rate of SNM in real water might stem from its increased levels of dissolved organic carbon (DOC) and impurities, thereby increasing competition with active species in comparison to deionized water. These results demonstrated the anti-interference stability exhibited by Mn/Co@N-biochar, further suggesting its immense potential for practical applications. Furthermore, we conducted experiments to validate the efficacy of the photocatalytic reaction system in eliminating other commonly encountered antibiotics. As depicted in Fig. 5i and Table S5, the biochar exhibited a removal efficiency of 52.3% for doxycycline, 11.3% for erbium, and 57.1% for CQP. Remarkably, the photocatalytic removal rates of Mn/Co@N-biochar improved significantly to 87.2%, 48.5%, and 99.0% for the aforementioned antibiotics, respectively. These results exemplify the activity and universality of the Mn/Co@N-biochar photocatalytic system in treating antibiotic pollutants found in water. The study illustrated the reusability and stability of SNM degradation by Mn/Co@N-biochar in cycling experiments. After six cycles (6 h/cycle), there was a slight decline in the effectiveness of photocatalysis by Mn/Co@N-biochar, yet the SNM removal rate remained at 91.0% (Fig. S6). This decline could be attributed to those substances generated during the degradation process blocked certain pores, resulting in a decrease in surface area and impacting active sites. Nonetheless, with the increase in the number of cycles from 3 to 6, the degradation efficiency remained relatively stable, highlighting the potential practical applications of Mn/Co@N-biochar. Furthermore, analysis of the FTIR (Fig. S7) and XRD (Fig. S8) indicated that there were no significant alterations in the surface functional groups and phase structure following 6 cycles.

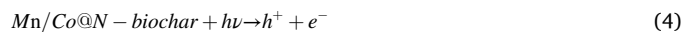
3.3. Mechanism of SNM degradation

In order to further elucidate the role of active species in the catalytic process of SNM elimination by Mn/Co@N-biochar, we conducted active

species capture experiments and EPR analysis. To trap specific active species, we introduced trapping agents, specifically 2 mM $K_2S_2O_8$, 1 mM L-histidine, 2 mM TBA, 0.1 mM BQ, and 2 mM EDTA-2Na into the reaction solution. These agents served the purpose of capturing e^- , 1O_2 , $\cdot OH$, $\cdot O_2^-$, and h^+ [54], correspondingly. As described in Fig. 6a, we observed that the addition of $K_2S_2O_8$, L-histidine, and EDTA-2Na had slight inhibitory effects on the photodegradation of SNM, reducing the removal from 99.0% to 94.0%, 81.0%, and 76.0% respectively. This suggested that the contributions of e^- and 1O_2 , and h^+ to SNM degradation were relatively small, accounting for 5.3%, 17.2%, and 23.4% respectively (see detailed calculation equations in SI). Conversely, the introduction of BQ and TBA displayed significant inhibitory impacts on SNM degradation, with the degradation efficiency dropping to 52.0% and 48.0%, respectively. These clearly suggested that $\cdot O_2$ and $\cdot OH$ were the main contributors to SNM degradation, accounting for 48.0% and 52.3% respectively. The creation of $\cdot OH$ and $\cdot O_2^-$ was observed by employing 5, 5 - dietyl-1- pyrroline -N- oxide (DMPO) as a chemical compound to capture free radicals. As shown in Fig. 6b and c, under dark conditions, neither $\cdot OH$ nor $\cdot O_2^-$ was produced in both the biochar and the Mn/Co@N-biochar. After 10 min of illumination, we observed four-peak typical DMPO-OH-signals[55] (Fig. 6b) and six-peak typical $\cdot O_2^-$ -signals[56] (Fig. 6c) in both the biochar and the Mn/Co@N-biochar. Moreover, the intensity of the Mn/Co@N-biochar signal exhibited a remarkable enhancement compared to that of biochar, implying that Mn/Co@N-biochar generated or converted more $\cdot OH$ and $\cdot O_2^-$. This observation consistently matched the outcomes of experiments trapping free radicals. In order to investigate the reaction mechanism of Mn, Co bimetallic co-catalysts, we conducted a comparative analysis of the diverse catalytic characteristics exhibited by biochar and Mn/Co@N-biochar through various photoelectronic characterization techniques. The charge transfer was measured with electrochemical impedance spectroscopy (EIS) and transient photocurrent profiles. The findings were presented in Fig. 6d, the impedance radius of Mn/Co@N-biochar was smaller than that of biochar, implying that the modified material reduced the impedance of charge transfer during the process of catalytic degradation[57], which could promote electron-hole pair separation. Fig. S9 demonstrated that Mn/Co@N-biochar displayed a stable and rapid photoresponse with higher photogenerated electron separation and migration capacity compared to biochar when subjected to repeated light conditions in a 50 s cycling cycle. Electron-hole pair separation rates of materials were evaluated using photoluminescence (PL). As depicted in Fig. S10, both materials exhibited similar emission peaks at 380 nm under 390 nm excitation[58]. Nevertheless, the emission intensity of Mn/Co@N-biochar exhibited a noteworthy reduction in comparison to that of biochar. This observation suggested that the integration of Mn and Co bimetallics conscientiously hindered the amalgamation of photogenerated electrons and holes, thereby enhancing the conductivity of charge transfer in Mn/Co@N-biochar, and leading to an increased utilization of electrons and improved efficacy of photocatalysis. Additionally, analysis of the LSV curves showed that the onset potential of Mn/Co@N-biochar was lower than that of biochar (Fig. 6e), suggesting improved conductivity at relatively small applied potentials due to the incorporation of Mn and Co and N doping, which enhanced carrier separation at the catalyst interface[59]. Furthermore, according to the results of XAS, it was discovered that the single atomic Mn and Co in Mn/Co@N-biochar display 4-fold coordination with N atoms. A potential optimization model was created for Mn/Co@N-biochar, as shown in Fig. S11. Fig. S12 displayed the projected density of states (PDOS) for Mn/Co@N-biochar and biochar, providing insight into their electronic structure analysis. Impurity states in Mn/Co@N-biochar were positioned close to the Femi energy level (the green dashed line), indicating that new impurity states in the gap of Mn/Co@N-biochar were generated by the *d*-orbitals of Mn and Co atoms and the *p*-orbitals of N[60]. This emphasized the crucial role played by the addition of Mn, Co, and N in influencing the electronic configuration of biochar. Furthermore, the

heightened concentration of Mn/Co@N-biochar near the Femi level suggested an improvement in catalytic activity. Moreover, DFT calculation results displayed the distribution of electron-holes on Mn/Co@N-biochar, blue signified the existence of holes while the green hue denoted the build-up of electrons (Fig. 6g). The pathway for electron transfer was evidently traced from the C and Mn atoms on the benzene ring to the Co atom.

According to the depiction provided in Fig. 6f, it could be observed that the Mn/Co@N-biochar facilitated a 49.0% mineralization of SNM, and resulted in a corresponding 99.3% removal of SNM. However, the mineralization capacity of biochar was merely 3.7%, leading to a 9.5% SNM removal. This difference suggested that Mn/Co@N-biochar exhibited significantly higher potential for mineralization compared to regular biochar. Nevertheless, the reason for the lower mineralization compared to the SNM removal rate lied in the incomplete decomposition of small molecules generated during the degradation of SNM[61]. The LC-MS results presented in Fig. 6h provided insights into the degradation pathway of SNM (*m/z* = 172.2). It could be inferred that the degradation initiated through two distinct pathways: C3-N11 cleavage and C6-S14 cleavage[62]. These pathways subsequently gave rise to two intermediates, namely 4-aminobenzenesulfonic acid (*m/z* = 174.19) and 6-hydrosulfonyl-113,3-thiazine (*m/z* = 163.93). As the process continues, the intermediates transformed further into small molecules such as maleic acid (*m/z* = 116.01), malonic acid (104.01), and oxalic acid (*m/z*=90.08). The decomposition process can proceed to complete mineralization, and finally SNM will be mineralized to H_2O and CO_2 [63, 64].



Based on the obtained results, a reaction mechanism was proposed (Fig. 6i). When the catalyst was exposed to visible light, it generated electron-hole pairs (Eq. (4)). The electrons produced were then swiftly transferred to the metal reaction centers, enhancing the activity of metal sites while creating numerous h^+ for oxidation reactions. This oxidation process triggered the production of $\cdot OH$ (Eq. (5)). The presence of Mn and Co on the surface of N-doped biochar led to charge redistribution, altering electron density in specific areas. The coordination bonds formed by Mn atoms and elements such as C and N provided electron transfer channels and promoted the directionality of electron migration from Mn to Co, resulting in the creation of electron-rich Co active sites and electron-poor Mn catalytic sites. In concrete terms, Mn increased the charge density of individual Co atoms, facilitating oxygen reduction and resulting in the production of more $\cdot O_2^-$ (Eq. (6))[65,66]. Conversely, the electron-poor Mn catalytic sites facilitated oxidation reactions, promoting the production of $\cdot OH$ (Eq. (7)). Additionally, efficient electron transfer enabled the regeneration of Mn^{2+} , contributing to improved results[67,68]. Consequently, the degradation of SNM could be achieved through redox reactions facilitated by electron cycling between Mn and Co sites. During this procedure, the generated radicals with reactivity serve the purpose of oxidizing the adsorbed SNM, causing the rupture of its C-S and C-N bonds. Following this, the phenolic and alcoholic intermediates undergo additional mineralization, resulting in the ultimate conversion into CO_2 and H_2O .

4. Conclusion

Highly dispersed and homogeneous Mn/Co@N-biochar catalysts supported on N-doped biochar were successfully prepared. The process involved implanting metal atoms Mn and Co into the N-doped biochar, allowing for the controlled synthesis of bimetallic single atoms and the

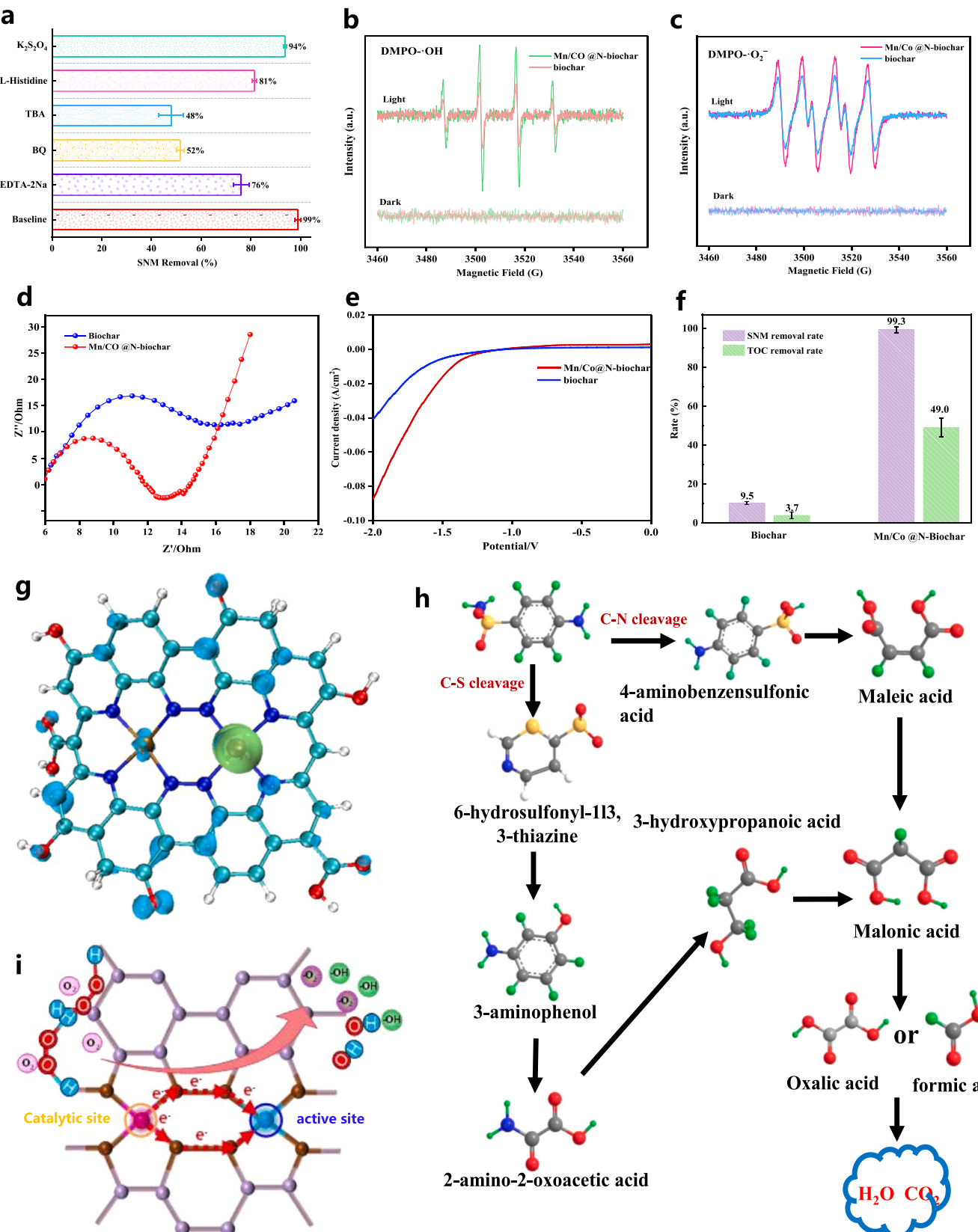


Fig. 6. (a) Effects of quencher on the degradation of SNM by Mn/Co@N-biochar. Signals generation of $\cdot\text{OH}$ (b) and $\cdot\text{O}_2$ (c) by biochar and Mn/Co@N-biochar. EIS curves (d) and LSV (e) for biochar and Mn/Co@N-biochar. (f) TOC for SNM degradation by biochar and Mn/Co@N-biochar. (g) Distribution of electron holes in Mn/Co@N-biochar calculated by DFT. (h) Pathways for degradation of SNM by Mn/Co@N-biochar. (i) Photocatalytic mechanism of SNM by Mn/Co@N-biochar.

homogeneous dispersion of the bimetallic central unit containing Co-N₄ and Mn-N₄ sites. Under visible light exposure, the synergistic interaction and efficient electron cycling of the Mn and Co sites in the Mn/Co@N-biochar catalysts effectively disrupted the C-S and C-N bonds in the SNM, thus leading to improved degradation efficiency. In SNM degradation experiments, the best photocatalytic activity and a degradation efficiency of 99.3% for SNM were achieved with a m(Mn):m(Co) ratio of 0.3:0.7. The study highlights the photocatalytic potential of Mn/Co@N-biochar as a single-atom bimetallic catalyst for treating SNM-polluted wastewater. It provides valuable insights into the creation and structure of dispersed bimetallic catalysts for wastewater treatment.

CRediT authorship contribution statement

Xin Wang: Writing – review & editing, Writing – original draft, Conceptualization. **Honghong Lyu:** Writing – review & editing, Project administration, Funding acquisition. **Jingchun Tang:** Validation, Supervision, Resources. **Pin Li:** Validation, Methodology, Data curation. **Ping Yan:** Software, Investigation, Formal analysis.

Declaration of Competing Interest

The authors declare that they have no known competing financial interests or personal relationships that could have appeared to influence the work reported in this paper.

Data Availability

Data will be made available on request.

Acknowledgments

The authors gratefully acknowledge financial supports for this work from the (1) Science Fund for Distinguished Young Scholars of Hebei Province (D2023202007), (2) National Natural Science Foundation of China (42177218), and (3) Science Fund for Distinguished Young Scholars of Tianjin (23JCJQJC00120).

Appendix A. Supporting information

Supplementary data associated with this article can be found in the online version at [doi:10.1016/j.apcatb.2024.124123](https://doi.org/10.1016/j.apcatb.2024.124123).

References

- [1] Y.-Z. Huo, R.-X. Guo, K.-X. Lin, et al., Insights into interface mechanism of three typical antibiotics onto the graphene oxide/chitosan composite: Experimental and theoretical investigation, *Chin. J. Chem. Phys.* 36 (2) (2023) 211.
- [2] C. Lai, M. Zhang, B. Li, et al., Fabrication of CuS/BiVO₄ (0 4 0) binary heterojunction photocatalysts with enhanced photocatalytic activity for Ciprofloxacin degradation and mechanism insight, *Chem. Eng. J.* 358 (2019) 891–902.
- [3] J. Cao, Y. Wang, L. Wang, et al., Na₃V₂(PO₄)₃@C as faradaic electrodes in capacitive deionization for high-performance desalination, *Nano Lett.* 19 (2) (2019) 823–828.
- [4] H. He, X. Jian, T. Zen, et al., Sulfur defect induced Cd_{0.3}Zn_{0.7}S in-situ anchoring on metal organic framework for enhanced photothermal catalytic CO₂ reduction to prepare proportionally adjustable syngas, *J. Colloid Interface Sci.* 653 (2024) 687–696.
- [5] H.W. Huang, D. Verhaeghe, B. Weng, et al., Metal halide perovskite based heterojunction photocatalysts, *Angew. Chem. Int. Ed.* 61 (24) (2022).
- [6] X. Gao, H. He, W. Zhu, et al., Continuously flow photothermal catalysis efficiently CO₂ reduction over S-scheme 2D/0D Bi₂O₃-I-OVs/Cd_{0.5}Zn_{0.5}S heterojunction with strong interfacial electric field, *Small* 19 (12) (2023) 2206225.
- [7] X. Wang, N. Fu, J.-C. Liu, et al., Atomic replacement of PtNi nanoalloys within Zn-ZIF-8 for the fabrication of a multisite CO₂ reduction electrocatalyst, *J. Am. Chem. Soc.* 144 (50) (2022) 23223–23229.
- [8] P. Attri, P. Garg, M. Chauhan, et al., Metal doped BiOCl nano-architectures (M-BiOCl, M = Ni, Mo, Cd, Co) for efficient visible light photocatalytic and antibacterial behaviour, *J. Environ. Chem. Eng.* 11 (2) (2023) 109498.
- [9] C. Gao, J. Low, R. Long, et al., Heterogeneous single-atom photocatalysts: fundamentals and applications, *Chem. Rev.* 120 (21) (2020) 12175–12216.
- [10] Z. Dong, L. Zhang, J. Gong, et al., Covalent organic framework nanorods bearing single Cu sites for efficient photocatalysis, *Chem. Eng. J.* 403 (2021) 126383.
- [11] S. Pang, C. Zhou, Y. Sun, et al., Natural wood-derived charcoal embedded with bimetallic iron/cobalt sites to promote ciprofloxacin degradation [J], *J. Clean. Prod.* 414 (2023) 137569.
- [12] Z. Lu, B. Wang, Y. Hu, et al., An isolated zinc–cobalt atomic pair for highly active and durable oxygen reduction, *Angew. Chem. Int. Ed.* 58 (9) (2019) 2622–2626.
- [13] A.M. Neris, W.H. Schreiner, C. Salvador, et al., Photocatalytic evaluation of the magnetic core@shell system (Co,Mn)Fe₂O₄@TiO₂ obtained by the modified Pechini method, *Mater. Sci. Eng.: B* 229 (2018) 218–226.
- [14] G.X. Zhang, D.L. Huang, M. Cheng, et al., Megamer of MOFs and g-C₃N₄ for energy and environment applications: upgrading the framework stability and performance, *J. Mater. Chem. A* 8 (35) (2020) 17883–17906.
- [15] H. He, X. Gao, K. Xu, et al., 1D/0D Z-scheme heterostructure of Bi₂S₃/CdXZn1-XS with strong interfacial electric field coupling enhanced mass transfer based on gas-liquid-solid micro interface contact for efficient photothermal synergistic catalytic CO₂ reduction to syngas, *Chem. Eng. J.* 450 (2022) 138266.
- [16] H. Yan, C. Lai, S. Liu, et al., Metal–carbon hybrid materials induced persulfate activation: Application, mechanism, and tunable reaction pathways, *Water Res.* 234 (2023) 119808.
- [17] M. Li, H. Huang, S. Yu, et al., Simultaneously promoting charge separation and photoabsorption of BiOX (X=Cl, Br) for efficient visible-light photocatalysis and photosensitization by compositing low-cost biochar, *Appl. Surf. Sci.* 386 (2016) 285–295.
- [18] H. Lyu, B. Gao, F. He, et al., Experimental and modeling investigations of ball-milled biochar for the removal of aqueous methylene blue, *Chem. Eng. J.* 335 (2018) 110–119.
- [19] B. Hui, H.J. Chen, C.F. Zhou, et al., Biochar aerogel-based electrocatalyst towards efficient oxygen evolution in acidic media, *Biochar* 4 (1) (2022).
- [20] H. He, X. Zhao, X. Jian, et al., Promoting photothermal catalytic CO₂ reduction of Cd₂In₂S₅/Cd_{0.3}Zn_{0.7}S heterojunction with encapsulated hydrogen evolution active site by accelerating charge transfer kinetics, *Chem. Eng. J.* 476 (2023) 146442.
- [21] Z. Yuan, H. He, X. Jian, et al., Synergistically enhanced photothermal catalytic CO₂ reduction by spatially separated oxygen and sulphur dual vacancy regulated redox half-reactions, *J. Alloy. Compd.* 968 (2023) 171959.
- [22] L.I.G.-L. Lu Z-F, X. Wang, et al., Rational construction of atomically dispersed Mn-Nx embedded in mesoporous N-doped amorphous carbon for efficient oxygen reduction reaction in Zn-air batteries, *J. ACS Sustain. Chem. Eng.* 10 (1) (2022) 224–233.
- [23] J. Dong, P. Li, X. Ji, et al., Electrons of d-orbital (Mn) and p-orbital (N) enhance the photocatalytic degradation of antibiotics by biochar while maintaining biocompatibility: A combined chemical and biological analysis, *J. Hazard. Mater.* 451 (2023) 131083.
- [24] C.A. Gorski, M. Aeschbacher, D. Soltermann, et al., Redox properties of structural Fe in clay minerals. 1. electrochemical quantification of electron-donating and -accepting capacities of ssmeities, *Environ. Sci. Technol.* 46 (17) (2012) 9360–9368.
- [25] H. Chen, G. Yurong, J. Li, et al., Insights into simultaneous adsorption and oxidation of antimonite [Sb(III)] by crawfish shell-derived biochar: spectroscopic investigation and theoretical calculations, *Biochar* 4 (3) (2022) 2524–2572.
- [26] X. Cui, Q. Ni, Q. Lin, et al., Simultaneous sorption and catalytic oxidation of trivalent antimony by *Canna indica* derived biochars, *Environ. Pollut.* 229 (2017) 394–402.
- [27] J. Zhan, B. Geng, K. Wu, et al., A solvent-engineered molecule fusion strategy for rational synthesis of carbon quantum dots with multicolor bandgap fluorescence, *Carbon* 130 (2018) 153–163.
- [28] M. Liu, N. Li, S.F. Cao, et al., A "pre-constrained metal twins" strategy to prepare efficient dual-metal-atom catalysts for cooperative oxygen electrocatalysis, *Adv. Mater.* 34 (7) (2022) 2107421.
- [29] T. Cui, Y.-P. Wang, T. Ye, et al., Engineering dual single-atom sites on 2D ultrathin N-doped carbon nanosheets attaining ultra-low-temperature zinc-air battery, *Angew. Chem. Int. Ed.* 61 (12) (2022) e202115219.
- [30] T.T. Sun, S. Zhao, W.X. Chen, et al., Single-atomic cobalt sites embedded in hierarchically ordered porous nitrogen-doped carbon as a superior bifunctional electrocatalyst, *Proc. Natl. Acad. Sci. USA* 115 (50) (2018) 12692–12697.
- [31] X.B. Zheng, J.R. Yang, Z.F. Xu, et al., Ru-Co pair sites catalyst boosts the energetics for the oxygen evolution reaction, *Angew. Chem. Int. Ed.* 61 (32) (2022) e202205946.
- [32] Q. Zhou, C. Song, P. Wang, et al., Generating dual-active species by triple-atom sites through peroxymonosulfate activation for treating micropollutants in complex water, *Proc. Natl. Acad. Sci. USA* 120 (13) (2023) e2300085120.
- [33] J. Li, M. Chen, D.A. Cullen, et al., Atomically dispersed manganese catalysts for oxygen reduction in proton-exchange membrane fuel cells, *Nat. Catal.* 1 (12) (2018) 935–945.
- [34] L. Zhang, J. Yang, A. Wang, et al., High performance ozone decomposition spinel (Mn,Cu)₃O₄ catalyst accelerating the rate-determining step, *Appl. Catal. B: Environ.* 303 (2022) 120927.
- [35] L. Guo, S. Hwang, B. Li, et al., Promoting atomically dispersed MnN₄ sites via sulfur doping for oxygen reduction: unveiling intrinsic activity and degradation in fuel cells, *ACS Nano* 15 (4) (2021) 6886–6899.
- [36] Y. Gao, Z. Han, S. Hong, et al., ZIF-67-derived cobalt/nitrogen-doped carbon composites for efficient electrocatalytic N₂ reduction, *ACS Appl. Energy Mater.* 2 (8) (2019) 6071–6077.
- [37] K. Asghar, M. Qasim, D. Das, Preparation and characterization of mesoporous magnetic MnFe₂O₄@mSiO₂ nanocomposite for drug delivery application, *Mater. Today.: Proc.* 26 (2020) 87–93.

[38] Q. Huang, F. Tong, Y. Gao, et al., Enhanced simultaneous arsenite oxidation and sorption by Mn-modified biochar: Insight into the mechanisms under optimal modification condition, *J. Environ. Chem. Eng.* 11 (3) (2023) 109612.

[40] K.S.W. Sing, Reporting physisorption data for gas/solid systems with special reference to the determination of surface area and porosity (Recommendations 1984), *Pure Appl. Chem.* 57 (4) (1985) 603–619.

[39] Z. Liu, M. He, L. Tang, et al., Dual redox cycles of Mn(II)/Mn(III) and Mn(III)/Mn(IV) on porous Mn/N co-doped biochar surfaces for promoting peroxyomonosulfate activation and ciprofloxacin degradation, *J. Colloid Interface Sci.* 634 (2023) 255–267.

[41] J. Zhang, J. Shao, X. Zhang, et al., Facile synthesis of Cu-BTC@biochar with controlled morphology for effective toluene adsorption at medium-high temperature, *Chem. Eng. J.* 452 (2023) 139003.

[42] Y. Sun, T. Zhou, W. Li, et al., Amino-functionalized alginate/graphene double-network hydrogel beads for emerging contaminant removal from aqueous solution, *Chemosphere* 241 (2020) 125110.

[43] Y. Cheng, X. Zhu, P. Yan, et al., Enhanced dual synergistic mechanism of adsorption and ozone triggering via biochar-derived zero-valent bimetal sites for water purification, *Appl. Catal. B: Environ.* 344 (2024) 123618.

[44] D. Ding, S. Yang, X. Qian, et al., Nitrogen-doping positively whilst sulfur-doping negatively affect the catalytic activity of biochar for the degradation of organic contaminant, *Appl. Catal. B: Environ.* 263 (2020) 118348.

[45] X. Mao, M. Wang, J. Li, et al., High atom utility of robust Ca-Co bimetallic catalyst for efficient Fenton-like catalysis in advanced oxidation processes, *Appl. Catal. B: Environ.* 331 (2023) 122698.

[46] Z. Chen, X. Xiao, B. Xing, et al., pH-dependent sorption of sulfonamide antibiotics onto biochars: Sorption mechanisms and modeling, *Environ. Pollut.* 248 (2019) 48–56.

[47] P. Wang, T. Zhou, R. Wang, et al., Carbon-sensitized and nitrogen-doped TiO₂ for photocatalytic degradation of sulfanilamide under visible-light irradiation, *Water Res.* 45 (16) (2011) 5015–5026.

[48] Y. Zheng, B. Cheng, W. You, et al., 3D hierarchical graphene oxide-NiFe LDH composite with enhanced adsorption affinity to Congo red, methyl orange and Cr (VI) ions, *J. Hazard. Mater.* 369 (2019) 214–225.

[49] J. Ali, A. Shahzad, J. Wang, et al., Modulating the redox cycles of homogenous Fe (III)/PMS system through constructing electron rich thiomolybdate centres in confined layered double hydroxides, *Chem. Eng. J.* 408 (2021) 127242.

[50] J. Qi, X. Yang, P.-Y. Pan, et al., Interface engineering of Co(OH)₂ nanosheets growing on the KNbO₃ perovskite based on electronic structure modulation for enhanced peroxyomonosulfate activation, *Environ. Sci. Technol.* 56 (8) (2022) 5200–5212.

[51] H. Xu, N. Jiang, D. Wang, et al., Improving PMS oxidation of organic pollutants by single cobalt atom catalyst through hybrid radical and non-radical pathways, *Appl. Catal. B: Environ.* 263 (2020) 118350.

[52] H. Zhang, X. Wang, X. Zhao, et al., Dolomite as a low-cost peroxyomonosulfate activator for the efficient degradation of tetracycline: performance, mechanism and toxicity evolution, *J. Water Process Eng.* 49 (2022) 103110.

[53] A. Takdastan, B. Kakavandi, M. Azizi, et al., Efficient activation of peroxyomonosulfate by using ferroferric oxide supported on carbon/UV/US system: a new approach into catalytic degradation of bisphenol A, *Chem. Eng. J.* 331 (2018) 729–743.

[54] G. Liu, G. Hou, X. Mao, et al., Rational design of CeO₂/Bi₇O₉I₃flower-like nanosphere with Z-scheme heterojunction and oxygen vacancy for enhancing photocatalytic activity, *Chem. Eng. J.* 431 (2022) 133254.

[55] P. Cui, C. Liu, X. Su, et al., Atomically dispersed manganese on biochar derived from a hyperaccumulator for photocatalysis in organic pollution remediation, *Environ. Sci. Technol.* 56 (12) (2022) 8034–8042.

[56] Z. Zhang, Z. Pan, Y. Guo, et al., In-situ growth of all-solid Z-scheme heterojunction photocatalyst of Bi₇O₉I₃/g-C₃N₄ and high efficient degradation of antibiotic under visible light, *Appl. Catal. B: Environ.* 261 (2020) 118212.

[57] X. Tian, T. Luo, Y. Nie, et al., New insight into a fenton-like reaction mechanism over sulfidated β -FeOOH: key role of sulfidation in efficient iron(III) reduction and sulfate radical generation, *Environ. Sci. Technol.* 56 (9) (2022) 5542–5551.

[58] P. Ding, H. Ji, P. Li, et al., Visible-light degradation of antibiotics catalyzed by titania/zirconia/graphitic carbon nitride ternary nanocomposites: a combined experimental and theoretical study, *Appl. Catal. B: Environ.* 300 (2022) 120633.

[59] B.T. Diroll, A. Brumberg, A.A. Leonard, et al., Photothermal behaviour of titanium nitride nanoparticles evaluated by transient X-ray diffraction, *Nanoscale* 13 (4) (2021) 2658–2664.

[60] H. Xu, D. Cheng, D. Cao, et al., A universal principle for a rational design of single-atom electrocatalysts, *Nat. Catal.* 1 (5) (2018) 339–348.

[61] Y. Xiao, H. Lyu, J. Tang, et al., Effects of ball milling on the photochemistry of biochar: Enrofloxacin degradation and possible mechanisms, *Chem. Eng. J.* 384 (2020) 123311.

[62] P. García-Muñoz, G. Pliego, J.A. Zazo, et al., Sulfonamides photoassisted oxidation treatments catalyzed by ilmenite, *Chemosphere* 180 (2017) 523–530.

[63] Y. Wu, H. Ji, Q. Liu, et al., Visible light photocatalytic degradation of sulfanilamide enhanced by Mo doping of BiOBr nanoflowers, *J. Hazard. Mater.* 424 (2022) 127563.

[64] K. Kokoszka, J. Wilk, E. Felis, et al., Application of UHPLC-MS/MS method to study occurrence and fate of sulfonamide antibiotics and their transformation products in surface water in highly urbanized areas, *Chemosphere* 283 (2021) 131189.

[65] H. Lyu, P. Li, J. Tang, et al., Single-atom Mn anchored on N-doped graphene oxide for efficient adsorption-photocatalytic degradation of sulfanilamide in water: Electronic interaction and mineralization pathway, *Chem. Eng. J.* 454 (2023) 140120.

[66] V. Giulimondi, S.K. Kaiser, A.J. Martín, et al., Controlled formation of dimers and spatially isolated atoms in bimetallic Au-Ru catalysts via carbon-host functionalization, *Small* 18 (15) (2022) 2200224.

[67] Q. Sun, M. Liu, K.Y. Li, et al., Synthesis of Fe/M(M = Mn, Co, Ni) bimetallic metal organic frameworks and their catalytic activity for phenol degradation under mild conditions, *Inorg. Chem. Front.* 4 (1) (2017) 144–153.

[68] L. Wang, M. Sun, S. Zhu, et al., Cu-Ni bimetallic single atoms supported on TiO₂@NG core-shell material for the removal of dibenzothiophene under visible light, *Sep. Purif. Technol.* 279 (2021) 119646.